A new approach to wavefront sensing: AI software with an autostigmatic microscope

Gaston Baudat[1], Robert E. Parks[2] and Benjamin Anjakos[3]

[1]Innovations Foresight, LLC., 4432 Mallard Point, Columbus Indiana, IN. 47201, USA
[1]Adjunct Research Professor, Wyant College of Optical Sciences, The University of Arizona, 1630 E. University Blvd., Tucson, Arizona 85721, USA

[2]Optical Perspectives Group, LLC. 7011 E. Calle Tolosa, Tucson, AZ 85750, USA

[3]Steward Observatory, The University of Arizona, Tucson, AZ 85750, USA

Abstract

The use of artificial intelligence (AI) software for wavefront sensing has been demonstrated in previous studies [1], [3]. In this work, we have developed a novel approach to wavefront sensing by coupling an AI software with an Autostigmatic Microscope (AM). The resulting system offers optical component and system testing capabilities similar to those of an interferometer used in double pass, but with several advantages. The AM is smaller, lighter, and less expensive than commercially available interferometers, while the AI software is capable of reading out Zernike coefficients, providing real-time feedback for alignment.

Our AI software uses an artificial neural network (NN) that is trained to output the Zernike coefficients, or any other relevant figures of merit, exclusively from synthetic data. The synthetic data includes random Zernike coefficients for a parametric description of the wavefront, noise, and a defocus error to avoid any stringent accuracy requirement. Once trained, the NN yields Zernike coefficients from a single frame of defocused intensity. The feedforward architecture of the NN enables swift output of Zernike coefficients, eliminating the need for iteration or optimization during run time.

Using the software with an AM allows for paraxial alignment of the object in the test cavity, with the real-time Zernike coefficients guiding the item into optimal alignment. This double pass test is not possible with most other types of wavefront sensors, as they are designed for single-pass use. Our results demonstrate that the test results obtained compare well with modeled results, and that errors in the AM can be removed by calibration, as in the case of interferometer transmission spheres. Furthermore, the simple defocused image of a source provides non-ambiguous phase retrieval, which competes with traditional wavefront sensors such as Shack-Hartmann (SH) sensors or interferometers. The AI software provides high dynamic range, sensitivity and precision [3]. This novel approach to wavefront sensing has significant potential for use in a wide range of applications in the field of optics.

Keywords: Artificial intelligence, machine learning, wavefront sensing, field-dependent wavefront sensing, multi-source wavefront sensing, autostigmatic microscope, low cost fast wavefront sensing.

1. INTRODUCTION

Wavefront (WF) sensing holds significant importance in the quantitative evaluation of optical systems. Its applications span numerous fields, including metrology, optical alignment, adaptive (AO) and active optics (aO), astronomy, as well as ophthalmology, among others. Common wavefront sensors, such as the Shack-Hartmann (SH) wavefront sensor and the curvature sensing wavefront sensor [1], primarily employ pupil or near-pupil space wavefront sensing methodologies.

The SH wavefront sensor necessitates the use of a lenslet array. However, these arrays can often be expensive and require precision in alignment. Moreover, the dynamic range of this sensor is restricted by the overlapping of images from adjacent sub-pupils.

On the other hand, curvature sensing [2] allows the reconstruction of the complete wavefront from two carefully defocused images of a planewave (a point source at infinity). However, the results can be susceptible to issues like noise and the initial input conditions, and it necessitates a setup capable of near-simultaneous data collection. Additionally, solving the irradiance transport equation with iterative numerical methods can encounter local minima and convergence problems, particularly when dealing with substantial aberrations. Also, the defocus must be sufficiently large to ensure it encompasses the caustic region for irradiance transport equation to be valid. As such, curvature sensing is classified as a near-pupil space WF sensing technique.

On the other hand, image space WF sensing provides an appealing alternative. It necessitates minimal or no additional hardware, leading to a unified optical path with the image plane. This feature eliminates the requirement for multi-path calibration and associated wavefront reconstruction residual errors. Phase diversity is a method commonly used for image space WF sensing. This approach hinges on at least two defocused images captured at distinct defocus positions near the focal plane, and it employs iterative phase estimation algorithms in real-time.

Single image WF sensing, using phase retrieval algorithms for a known source, typically relies on iterative error reduction techniques, such as the Gerchberg-Saxton (GS) algorithm. However, the GS algorithm often struggles to achieve the exact solution after iterations, resulting in approximations. Furthermore, its convergence tends to be rather slow, typically characterized by plateaus where the error remains almost constant across many iterations.

In this paper, we introduce an image space WF sensing approach using artificial intelligence, denoted as AIWFS [1]. It is capable of performing phase retrieval from a single defocused image, even under noisy conditions. This method boasts three highly desirable features:

- Requires only a single image.
- Fast processing (no iteration) at run time.
- Whole field WF sensing.

An artificial NN forms the core of our method and is trained solely on synthetic data. This data consists of simulated aberrated and defocused images, primarily utilizing point sources at, or near, infinity that essentially produce plane waves. While we could consider more complex sources like spherical waves or extended sources, for the purpose of this paper, we focus specifically on scenarios involving plane waves.

These sources can be conceptualized as either artificial or real stars, aligning with our original intent for this technology: to aid in the alignment of telescopes or aO, as well as AO.

The images we utilize are computed using scalar diffraction theory. Our NN serves as a function approximation tool, mapping single defocused images to their respective wavefronts, commonly expressed in Zernike annular polynomial coefficients. As a result, during runtime, there is no need for iterations, optimizations, or concerns about convergence for phase retrieval calculations. All the complex computations have been carried out during the training phase of the NN. When presented with a new single-defocused image of a star, the NN swiftly provides the related wavefront data (i.e., the Zernike annular polynomial coefficients). The chosen NN's feed-forward structure enables fast phase retrieval calculations, aligning well with video-rate wavefront sensing applications.

Inherently, this method can access wavefronts in the entire field simultaneously when presented with a single defocused star field image. For the scope of this paper, we consider only monochromatic sources. This choice isn't a limitation of the technology but a strategy to expedite calculations. In real-world applications, we often deal with color filters or lasers. In scenarios involving color filters, the monochromatic calculations stay relevant when the filters have a bandwidth up to proximately 100nm or less.

Firstly, we will outline the methodology and results within the context of telescopes. Following this, we will explore its application in an AM setup, in the form of a Point Source Microscope (PSM). The latter bears significant resemblance to

a telescope operating in double pass mode when an artificial star is utilized.

2. METHODOLOGY

2.1 Background and concept

The far field, intensity distribution of the monochromatic point spread function (PSF) is given by the square modulus of the two-dimensional Fourier transform of the complex pupil function:

$$\mathrm{PSF}(u,v) = |\mathcal{F}_{2D}\{(P(x,y)\}|^2 \tag{1}$$

The complex pupil function $P(x,y)$ contains information about the shape of the pupil, the transmission function and optical phase in the pupil. In general, the complex pupil function is defined as follows:

$$P(x,y) = p(x,y)e^{j\varphi_p(x,y)} \tag{2}$$

where: $p(x,y)$ = pupil amplitude transmission function,
$\varphi_p(x,y)$ = the pupil phase function = $2\pi W(x,y)/\lambda$, and
$W(x,y)$ = wavefront departure from the reference sphere.

With the required scaling factors, the radial PSF becomes:

$$\mathrm{PSF}(r') = \frac{I_0}{(\lambda f)^2}|T(\rho)|^2_{\rho=r'/\lambda f} \tag{3}$$

Where:
I_0 = the irradiance in power/area incident on the pupil,
λ = operating wavelength,
f = focal length,
r'= radial coordinate in the focal plane,
$T(\rho) = \mathcal{F}\{P(r)\}$ = Radial Fourier transform (Hankel transform) of the complex pupil function.

Using equation 3, we can readily compute the monochromatic PSF for any phase distribution in the pupil. As demonstrated by Baudat [1], it is possible to normalize and sample the input data for general applicability across various optical systems.

Practically speaking, it's beneficial to employ radial annular Zernike polynomials to construct a selective orthogonal set of aberrations most suitable for the task at hand. For instance, this methodology is particularly advantageous for aligning diverse types of optics, such as two-mirror telescope systems. Here, minimizing on-axis coma and balancing off-axis astigmatism ensures optimal secondary mirror alignment, and reducing spherical aberration optimizes mirror spacing. Additionally, the ability to identify astigmatic and trefoil terms proves valuable for enhancing field performance and detecting potential mechanical mounting stress. For these tasks, it is adequate to train the NN to identify only the nine Zernike terms listed in Table 1.

It's important to clarify that this is not a constraint of the method itself. The methodology could be trained to recognize higher-order Zernike terms and atmospheric seeing parameters. The AIWFS technology has been used for Zernike polynomials up to the 8th radial order. The only limitations relate to the size of the NN database and the computing time required to process the input data and train the system. In most applications, we can disregard the piston term (time-incoherent light, z0=0) as well as the tilt and tip (z1=0 & z2=0) of the wavefront. This is because we center the defocused image during the preprocessing step before feeding it into the NN.

Name	Index	Radial Annular Polynomials $0 < r \leq 1 \qquad 0 < \epsilon \leq 1 \qquad 0 \leq \theta \leq 2\pi$
Defocus	Z_3	$(2r^2 - 1 - \varepsilon^2)/(1 - \varepsilon^2)$
Vertical astigmatism	Z_4	$\left(r^2/\sqrt{1+\epsilon^2+\epsilon^4}\right) cos(2\theta)$
Oblique astigmatism	Z_5	$\left(r^2/\sqrt{1+\epsilon^2+\epsilon^4}\right) sin(2\theta)$
Horizontal coma	Z_6	$[3r^3(1+\epsilon^2) - 2r(1+\epsilon^2+\epsilon^4)]/\left[(1-\epsilon^2)\sqrt{(1+\epsilon^2)(1+4\epsilon^2+\epsilon^4)}\right] cos(\theta)$
Vertical coma	Z_7	$[3r^3(1+\epsilon^2) - 2r(1+\epsilon^2+\epsilon^4)]/\left[(1-\epsilon^2)\sqrt{(1+\epsilon^2)(1+4\epsilon^2+\epsilon^4)}\right] sin(\theta)$
Primary spherical	Z_8	$(6r^4 - 6r^2(1+\epsilon^2) + 1 + 4\epsilon^2 + \epsilon^4)/(1-\epsilon^2)^2$
Oblique trefoil	Z_9	$\left[r^3/\sqrt{1+\epsilon^2+\epsilon^4+\epsilon^6}\right] cos(3\theta)$
Vertical trefoil	Z_{10}	$\left[r^3/\sqrt{1+\epsilon^2+\epsilon^4+\epsilon^6}\right] sin(3\theta)$
Secondary spherical	Z_{15}	$[(20r^6 - 30r^4(1+\epsilon^2) + 12r^2(1+3\epsilon^2+\epsilon^4) - (1+9\epsilon^2+9\epsilon^4+\epsilon^6)]/(1-\epsilon^2)^3$

Table 1. Definition of the nine radial annular Zernike terms using the Wyant-Creath [8] numbering convention, following Mahajan's definitions. These are the basic common terms used for generating synthetic data and for training the AI system described here with $\varepsilon = 0$ for the PSM experiments.
In some context higher orders terms have been consider up to the Zernike radial order 8.

2.2 Data generation and training

The synthetic data, specific to a given optical imaging system (such as a telescope or a PSM), is computed using scalar diffraction theory and Fast Fourier Transform (FFT) to model the defocused image. For obstructed circular entrance pupils, we utilize the central obstruction parameter, denoted as $0<\varepsilon\leq1$. This parameter signifies the degree of obstruction as a percentage of the pupil diameter, D. This concept becomes particularly significant when evaluating a centered circular secondary mirror in the context of a telescope. Although this paper focuses on circular apertures (axially symmetric systems), the most common type, other shapes can also be accommodated.

We have chosen to use the Zernike radial annular polynomials for articulating the WF phase errors (aberrations) across the entrance pupil. In relevant scenarios, we also consider the Fried parameter or coherence length (r0) for quantifying the strength of Earth's atmospheric turbulences, often referred to as 'seeing.' Various levels of noise are incorporated into the synthetic data to account for sensor, electronic, and shot noise, as well as scintillation.

To train the ANN, we generate defocused images across predefined ranges of the Zernike coefficients, in accordance with the application and aberration budgets, as well as r0 values where applicable. Alternate strategies could involve directly sampling an aberrated wavefront. In such a case, the NN outputs would be the sampled wavefront itself, instead of the Zernike coefficients or other aberration terms. In this paper, we've opted for a parametric approach, which describes the WF error through the Zernike radial annular polynomials. While not a limitation of the method, we are primarily concerned with optical alignment and thus focus on the lower 3rd order aberrations, under the assumption of near-perfect optical surface figures. Monitoring these low-order aberrations is sufficient for our task, though higher-order aberrations could be taken into account, particularly when measuring optical surface figures and roughness.

The NN training phase utilizes three datasets. The first is the learning dataset, which serves to optimize the NN (synaptic weights). This dataset is typically the largest, with anywhere from 500,000 to 1,000,000 samples or more. The second, the validation dataset, monitors the NN's generalization performance during the training process to prevent overlearning,

containing between 10,000 to 50,000 samples. The third is the test dataset, utilized post-training to assess the model's generalization capability, performance, and accuracy. All datasets are generated from the same independently identically distributed uniform random variable simulations, spanning the range of Zernike coefficients and r0 values, when under seeing limited conditions. Figure 1 below illustrates the basic steps involved in loading and training the neural network.

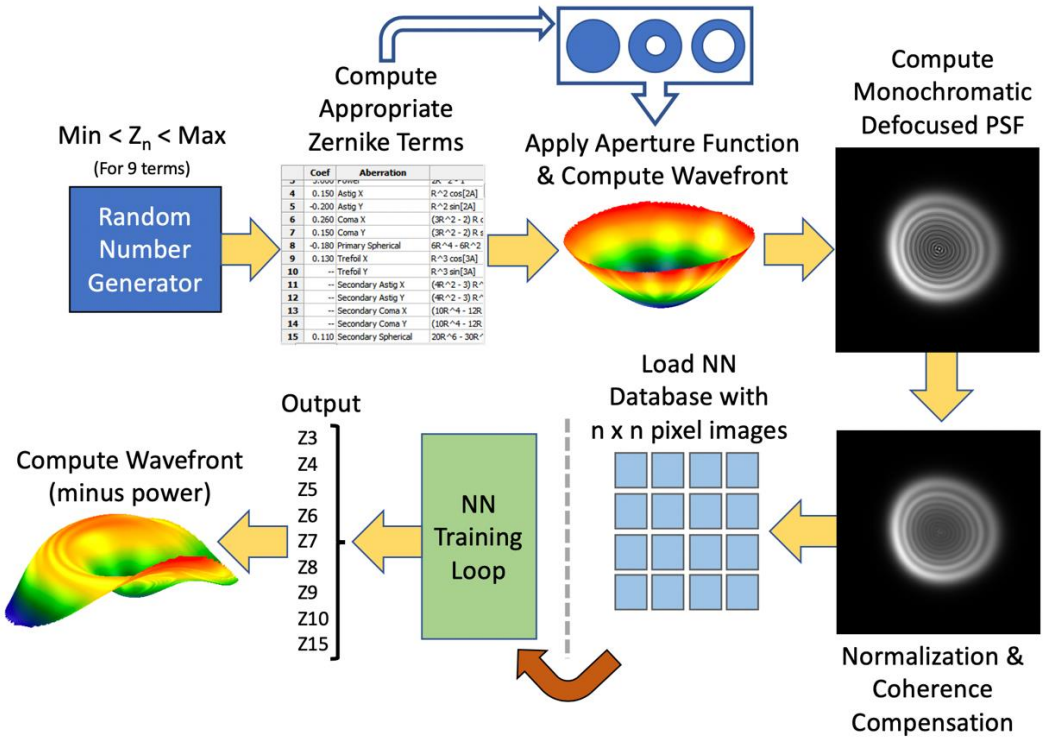

Figure 1. The basic steps for loading data and training the neural network (NN) to recognize 9 Zernike terms.

2.3 Uniqueness of Phase Retrieval

Beside piston z0 & the spatial shifts tilt & tip (z1, z2), which all are set to zero in our application, phase retrieval faces a last trivial ambiguity, the conjugate inversion, as shown from the pupil function $P(x, y)$ cross-correlation, the OTF:

$$\mathrm{OTF}(\zeta, \eta) = P(x,y) \otimes P(x,y) = P^*(-x,-y) \otimes P^*(-x,-y) \tag{4}$$

Where * denotes the complex conjugate operation.
There are 2 pupil functions $P(x, y)$ leading to the same PSF:

$$P(x,y) = p(x,y)e^{j\varphi_p(x,y)} \tag{5}$$

$$P^*(-x,-y) = p(-x,-y)e^{-j\varphi_p(-x,-y)} \quad \text{conjugate inversion} \tag{6}$$

For a circular pupil p(x,y) is a real even function, the only ambiguity we have to handle is for the phase $\varphi_p(x,y)$. This issue can be tackled by introducing a known phase modulation. The most straightforward and simplest method involves adding a defocus bias (Z3). While other types of modulation, such as spherical aberrations, could be used, in this paper, we confine our analysis to the application of defocus bias.

Figure 2 presents a perfect PSF in the left images, and two aberrated PSFs with +3 waves (center images) and -3 waves (right images) of primary spherical (Z8) aberration respectively. The top row represents the in-focus situation (z3=0) with no phase modulation. The identical appearance of the two aberrated PSFs indicates the loss of phase sign. This ambiguity is resolved by adding 10 waves of defocus (Z3) bias, which acts as the modulation, as seen in the bottom row. Here, the two aberrated PSFs are clearly distinguishable. The requirement is a defocus bias that is significant enough to ensure there is always some degree of defocus with a known sign, even after considering factors like defocusing bias accuracy, field curvature, sensor tilts, and any other sources of defocus error. Contrary to curvature sensing, we don't need to be beyond the caustic region to fully recover the WF. Actually, we consider any defocus error as an aberration similar to any other, and we train the NN within a predefined range of defocus error.

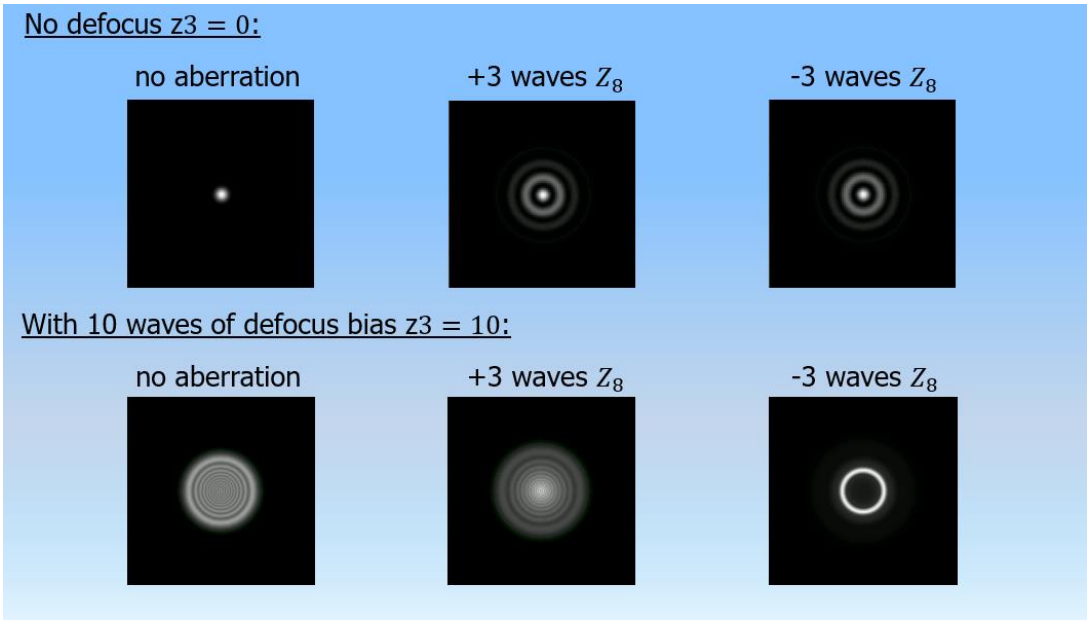

Figure 2. The top row corresponds to the in-focus situation (z3=0) with no phase modulation. The two aberrated PSFs, with respectively +3 (center) and -3 (right) waves of primary spherical (Z8), are identical, indicating that the phase sign has been lost. This ambiguity is resolved by adding 10 waves of defocus (Z3) bias, serving as the modulation, as observed in the bottom row.

3. EXPERIMENTS WITH TELESCOPES

Several experiments have been carried out in the lab in double pass, and on the sky using real stars under seeing limited conditions [3].

3.1 Comparison with a Shack Hartmann wavefront sensor on an optical bench

A compact refractor telescope, see figure 3, designed as an optical bench has been assembled, incorporating a pellicle beam splitter and a pinhole located in the telescope's focal plane, serving as an artificial star. The PSF images are captured either in or out of focus by a CMOS camera (ZWO ASI 1600MM). To restrict the light's bandwidth, we employed a red filter, thereby facilitating the use of a monochromatic model for training the ANN. Telescope features a single achromat with a clear aperture of 24mm and focal length of 300mm, which results to a f/12.5 system. The pinhole is illuminated with a white LED and a diffuser.

A good flat mirror is positioned in front of the telescope aperture for double-pass measurements. The CMOS camera can be substituted with a 40x40 lenslet SH wavefront sensor from ALCOR SYSTEM, paired with its corresponding collimating lens to re-image the pupil. Whether using the camera for AIWFS or the SH sensor, the same light source and red filter are utilized, ensuring consistent working conditions at the same point on the optical path. This minimizes any discrepancy

between the two wavefront measurements. The SH exposure time was set at 200ms to ensure sufficient signal-to-noise ratio (SNR) for each microlens, while the AIWFS CMOS camera exposure was set at 10ms. This setting is consistent with video rate and adaptive optics (AO) applications under seeing conditions.

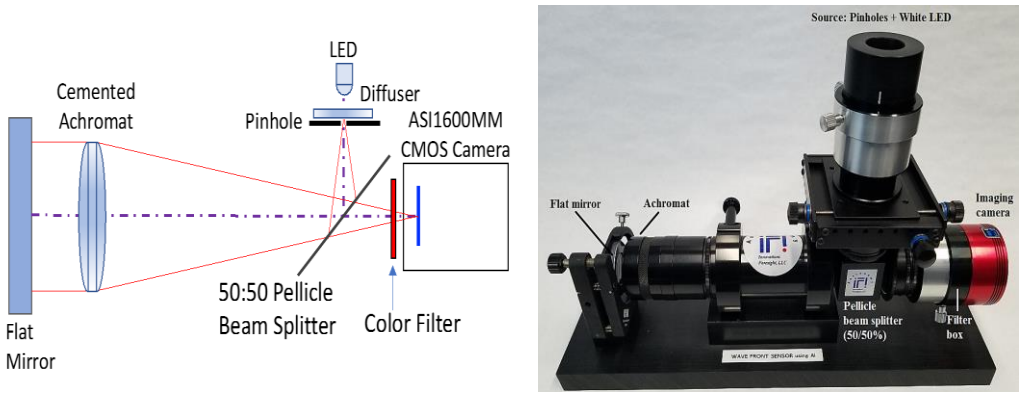

Figure 3. 24mm f/12.5 double pass refractor telescope with a pinhole, as an artificial star, and its CMOS camera

The table 2 shows the Strehl's ratio (SR), the WF errors, as well as the Zernike coefficients for the SH and the AIWFS approaches @650nm. They are in very good agreement, the maximum difference on the Zernike coefficient is 0.002 wave, or 1.3nm for astigmatism and secondary spherical.

Measurements (Zernike: Wyant's index)	**Shack-Hartman**	**AIWFS**
Strehl's ratio (SR)	0.9864	0.9869
RMS FW error	0.017 wave (11.2nm)	0.018 wave (11.7nm)
PV FW error	0.127 wave (82.2nm)	0.116 wave (75.4nm)
Primary Astigmatism Z4+Z5	0.039 wave (25.0nm)	0.041 wave (26.7nm)
Primary Coma Z6+Z7	0.002 wave (1.5nm)	0.003 wave (2nm)
Primary Trefoil Z9+Z10	0.005 wave (3.5nm)	0.006 wave (3.9nm)
Primary Spherical Z8	0.002 wave (1.4nm)	0.002 wave (1.3nm)
Secondary Spherical Z15	0.021 wave (13.4nm)	0.019 wave (12.4nm)

Table 2. Comparisons on a refactor telescope optical bench between a SH WF sensor and the AIWFS approach @650nm (monochromatic model)

3.2 Wavefront analysis using an actual star under seeing limited conditions

This work was principally driven by the application of aligning, also known as collimating, multi-mirror telescopes using stars as a source. Two additional considerations surpassing the laboratory measurements presented here apply to this application [3].

Firstly, the AIWFS system must be trained to handle an obscured aperture, and depending on the optical configuration, this might also involve training for additional structures in the pupil, such as spider vanes.

The second consideration pertains to atmospheric seeing. Kolmogorov's turbulence theory provides the relationship between Fried's atmospheric coherence length parameter r0 and the Full Width at Half Maximum (FWHM), denoted as β, of the seeing-limited star image, expressed in radians.

$$\beta \cong 0.98\ \lambda/r_0 \tag{7}$$

The blurred stellar profile is best represented by a Moffat function. However, for most practical applications, a Gaussian function offers satisfactory results when calculating defocused star images and it is particularly easy to implement. Using equation 7, the seeing-induced Gaussian kernel width, represented by σ and measured in radians, can be determined as follows:

$$\sigma = \frac{\beta}{2\sqrt{2\ln(2)}} \cong 0.42\ \frac{\lambda}{r_0} \tag{8}$$

Under the sky, data can be captured with exposure times ranging from a few seconds up to 100 seconds. This produces a time-averaged PSF that can be matched by the AI system to a database of low-pass Gaussian filtered defocused star images. These images are calculated using equation 3 and blurred according to the bandwidth limit imposed by equation 8. The AI system can be trained not only to report the desired Zernike terms but also to output the Fried's parameter r0, for monitoring seeing quality.

Figure 4 showcases the 2D WF heat maps (illustrated with peaks in red and valleys in blue), alongside the corresponding PSFs derived from an actual star (with r0 = 4.9 cm at 656nm). These were captured using a Schmidt-Cassegrain telescope with a 559mm aperture at an f/9.1 ratio. The heat map and PSF on the left were obtained through a 40x40 lenslet Shack-Hartmann wavefront sensor supplied by ALCOR-SYSTEM. Conversely, the figures on the right display the results produced by the AIWFS approach, which utilized a single defocused image of an actual star captured by a ZWO ASI1600MM monochrome CMOS camera. In both cases, data was collected using a red filter featuring a central wavelength of 656nm, a bandwidth of 6nm, and an exposure time of 5 seconds. These measurements were conducted at the DOMAS–RGNext facility in Patrick Space Force Base, Florida, with official disclosure permission granted by Range Generation Next.

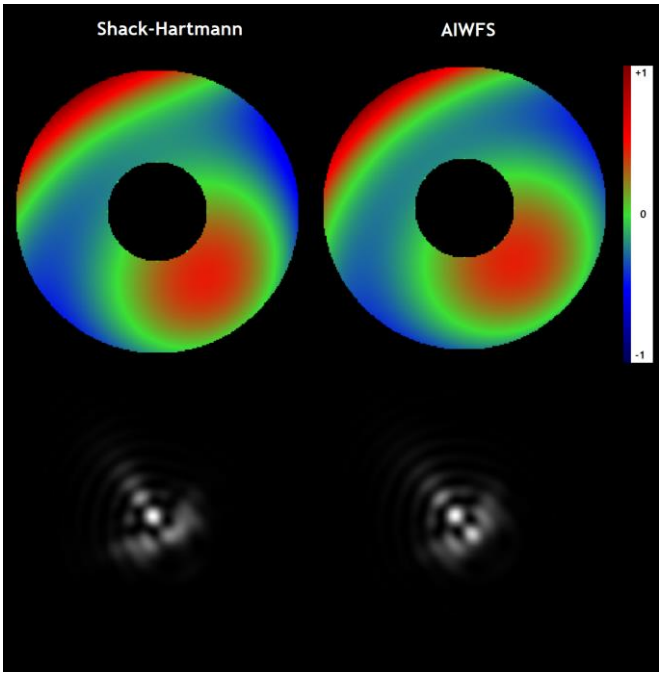

Figure 4. 559mm aperture at f/9.1 Schmidt-Cassegrain telescope WF heat plots and PSFs using an actual star (r_0 = 4.9 cm). Left with a Shack-Hartmann, right with the AWIFS approach. 5 seconds exposure @656nm for both cases.

Table 3 below details the basic aberrations at 656nm, presented in terms of Zernike annular polynomial coefficients. Despite the challenging seeing conditions and short exposure time (5s), the maximum discrepancy is only 0.06 waves, or 39nm, equivalent to a root mean square (rms) of 0.01 waves, or 6.6 nm rms. For comparison, the diffraction limit (SR = 80%) corresponds to a rms WF error of roughly 0.075 waves rms, or 49nm rms, which is about 7 times greater than the observed maximum difference. The data from both sets demonstrates a solid match, implying that this telescope may require some optical realignment.

Measurements (Zernike: Wyant's index)	**Shack-Hartman**	**AIWFS**
Strehl's ratio (SR)	0.14	0.19
RMS FW error	0.277 wave (182nm)	0.271 wave (178nm)
Primary Astigmatism Z4+Z5	0.96 wave (630nm)	0.91 wave (597nm)
Primary Coma Z6+Z7	0.98 wave (643nm)	0.98 wave (643nm)
Primary Trefoil Z9+Z10	0.05 wave (33nm)	0.11 wave (66nm)
Primary Spherical Z8	0.05 wave (33nm)	0.11 wave (66nm)

Table 3. Comparison between a SH WF sensor and the AIWFS approach under seeing-limited conditions on a 559mm f/9.1 Schmidt-Cassegrain telescope @656nm. The data disclosure was authorized by Range Generation Next at Patrick Space Force Base, Florida.

4. AUTOSTICMATIC MICROSCOPE

4.1 Description and concept

The Point Source Microscope (PSM) is an autostigmatic microscope (AM) [4] that also functions as an autocollimator and a reflection type inspection microscope [5]. As an autostigmatic microscope the PSM is used primarily for the alignment of optics by precisely locating the centers of curvature of optical surfaces with a lateral resolution of < 1 μm. When the PSM is focused at the center of curvature of a surface or optical system it simulates the use of an interferometer in a double pass test, the only difference being the PSM images the very small focal spot while the interferometer images the pupil of the surface being tested. The light path of the PSM focused at the center of curvature (CC) of a sphere is shown in the figure 5.

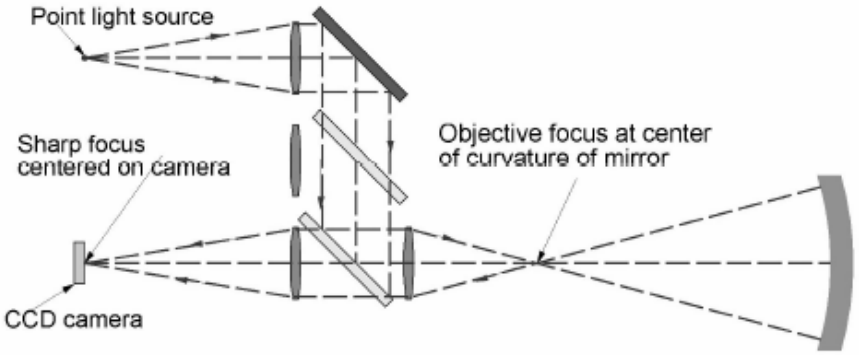

Figure 5. Light path in the PSM focused at the center of curvature of a spherical mirror to show the similarity with a double pass interferometer test setup

Because the optical setup is identical to using an interferometer it made sense to see if the PSM could be used as a WF sensor by simply adding additional sophisticated software implementing the AIWFS technology. There are at least 2 obvious optical advantages in addition to some hardware and cost advantages over using an interferometer. Optically, there are situations where aberrations are the only reasonable method of alignment such as aligning a parabola to a return flat mirror. Under most situations this type of alignment is impossible to do looking at centers of curvature and foci so minimizing aberrations is the only choice possible. The other optical advantage is that if a surface has been distorted in assembly being able to measure the effect on the WF during alignment means that corrective action is possible. This saves finding the defect during a final test and having to scrap or rework the assembly.

4.2 Modelization and specificity

The AIWFS technology has predominantly been applied to the alignment and evaluation of telescope optics, utilizing either actual or artificial stars, via a dedicated software called SkyWave (SKW). SKW serves as a metrology tool that detects defocused stars in user-provided images (monochrome FITS file format) and feeds this information into a specialized NN, or mathematical model, specifically designed and traained for a given telescope. The software computes all the essential Zernike coefficients (typically third-order aberrations) and provides quantitative analysis and data, including the PSF, MTF, and EE, as well as field-dependent aberration maps. In this scenario, the incoming light is essentially a plane wave, illuminating the entrance pupil uniformly. Figure 6 depicts a pair of SKW screenshots analyzing a star field from a single FITS image.

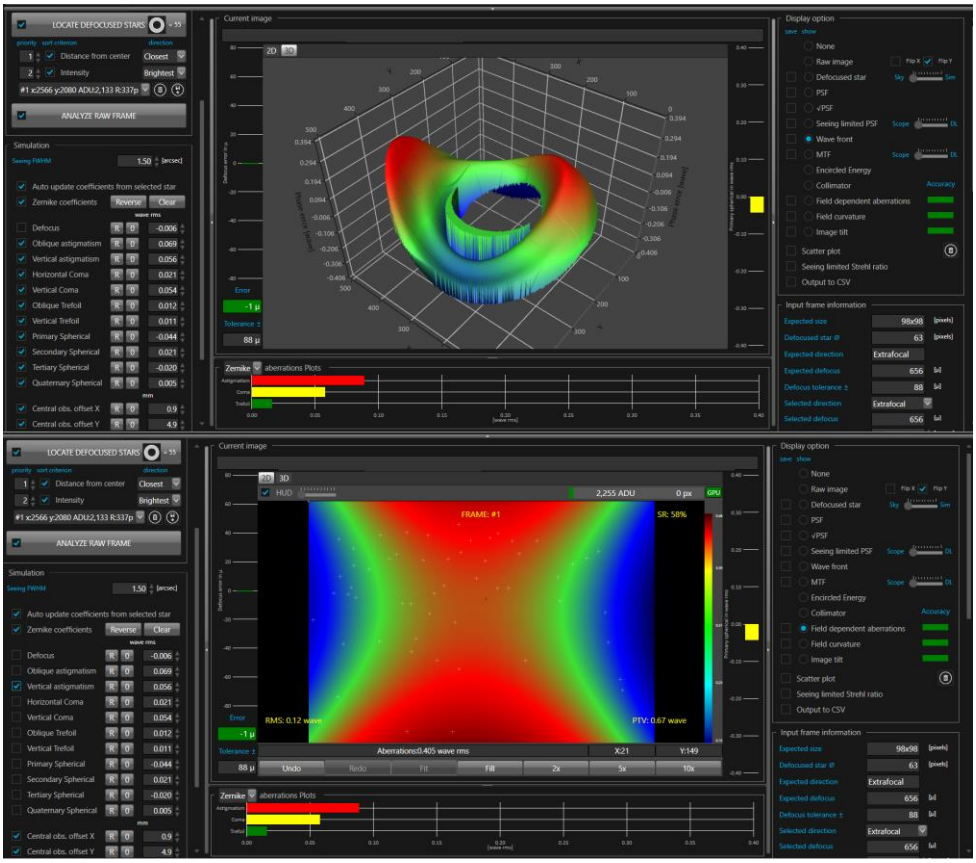

Figure 6. Two screenshots from SkyWave (SKW). The top image showcases a 3D wavefront of a star located near the center of the star field image. The bottom image displays the map of the vertical primary astigmatism Zernike annular coefficient across the entire field, computed using 55 stars throughout the image.

In order to evaluate the AIWFS technology with the PSM and SKW basic adjustments are required. The strategy of reusing SKW is beneficial as it provides a rapid prototyping solution and proof of concept before considering a more dedicated software implementation for the PSM. However, this choice also presents some limitations.

SKW, when calculating WF errors from a single defocused image of a star (be it real or artificial) for an astronomical telescope, relies on a model of an optical system that differs significantly from what is present in the PSM. These differences were not entirely evident at the outset. For a telescope, starlight uniformly illuminates the entrance pupil under all conditions, while in the PSM, the illumination originates from the free space end of a single-mode optical fiber. This creates a Gaussian intensity distribution with a Numerical Aperture (NA) of 0.1, incident on a collimating lens with a 30 mm effective focal length (efl), resulting in a beam waist of 3mm. The lens is stopped at 8mm, leading to a truncated Gaussian beam. This variation in illumination implies that the NN must be trained for this case, which constitutes a model distinct from that of the telescope.

Another distinction lies in the location of the effective stop in each case. With a telescope, the f-number (f/#) of the cone of light incident on the camera remains constant, whether the telescope is focused on a star or defocused by moving the camera further from the secondary or objective to produce the out-of-focus image utilized by SKW. The situation in the PSM is similar if a spacer is added to defocus the camera. However, if the defocus is created by adjusting the PSM's

proximity to the test surface, thereby generating a defocus bias aligned with the software's expectations, the degree of necessary adjustment is contingent on the focal length or magnification of the microscope lens in use.

This same requirement means that we must use an objective on the PSM that underfills the surface under test. Otherwise, the pupil of the surface would determine the f/# of the light cone reaching the camera. This means that the magnitude of the aberrations will be less than the total error in the surface being tested in all cases. This is not a problem when aberrations are used for alignment because for alignment the goal is to find the alignment that minimizes the aberrations.

The use of the SKW software introduces another consideration, paralleling the case of utilizing an interferometer. Neither the optics in an interferometer nor those in the PSM are perfect. In both situations, the instruments need calibration for optimal performance. Just as in the interferometer scenario where the numerical aperture (NA) of the transmission sphere acts as the stop, the Random Ball Test [6] could be the most suitable method for calibrating the PSM, where the NA of the objective limits the cone of light reaching the camera. Ultimately, the software and the corresponding mathematical model learned by the NN could be appropriately parameterized to accommodate the characteristics of the surface being analyzed.

Despite the inherent limitations and differences when applying SKW with a PSM, the initial results are highly encouraging. They suggest that AIWFS can be effectively implemented with a PSM for optical part alignment and WF sensing across diverse applications. This approach offers a unique, compact, and cost-effective solution for obtaining quantitative data on optical aberrations and WFs, thereby eliminating the need for an interferometer or dedicated wavefront sensors.

4.3 Test and results

We established an optical setup utilizing a PSM and a spherical concave mirror with a 100mm radius. To ensure full illumination of the mirror under all test conditions, we selected a microscope objective with an NA of 0.1. The stop is positioned at the level of the PSM's collimation lens, resulting in an 8mm beam. Given the PSM tube lens has an effective focal length (efl) of 100mm, this corresponds to an f/12.5 system. There are two methods to defocus the image, as discussed in the previous section: one involves adding a spacer in front of the PSM camera, thus shifting the image plane away from the tube lens focal plane; the other involves moving the PSM away from the mirror's CC. Equation 9 outlines the necessary spacing S for the former approach.

$$S = B16\sqrt{3}\lambda f\#^2 \tag{9}$$

In Equation 9, B represents the defocus bias or the phase modulation, λ represents the wavelength, and f# denotes the f-number of the imaging optics. For the PSM, we set λ at 640nm and f# at 12.5 (tube lens). The standard SKW mathematical models are trained with B set to 4.5 wave rms, which leads to a spacing of 12.471mm.

In the second approach, the PSM - initially focused at the mirror's center of curvature (CC) - is shifted away through axial translation by a certain ΔZ distance, in either direction. In the first approximation, there's a simple relationship outlined in Equation 10 between ΔZ and the motion of the image plane ΔI on the PSM's camera side.

$$\Delta I = 2\left(\frac{f\#_t}{f\#_0}\right)^2 \Delta Z \tag{10}$$

Where $f\#_t$=12.5 represents the PSM's tube lens f-number which images the beam onto the camera, and $f\#_0$ refers to the f-number of the PSM's microscope objective illuminating the spherical mirror, or any other target of interest. If the PSM is moved closer to the mirror, this results in an intra-focal defocused image.

For a microscope objective NA=0.1, in the air, $f\#_o = 5$, resulting to a $\Delta Z = \frac{12471}{2}\left(\frac{5}{12.5}\right)^2 = 0.998\text{mm}$ for 4.5 wave rms of defocus bias ($\Delta I = 12.471\text{mm}$).

A more precise Zemax simulation of the complete PSM optics suggests an axial translation, ΔZ, of 1.215mm in this context (B=4.5 waves rms). As long as the PSM's axial translation from the mirror's CC remains much smaller than the mirror's radius, we should expect a linear relationship between the defocus Zernike coefficient z3 and ΔZ, with a slope of 4.5/1215

= 0.0037 wave rms of defocus change per micron of PSM axial translation. The smaller the mirror's radius, the smaller the $f\#_0$ of the required PSM's microscope objective for full illumination of the mirror. This, in turn, leads to more sensitive detection of any axial translation from the coefficient z3 value provided by SKW, since the slope of equation 10 becomes steeper. This sensitivity is also applicable for other aberrations in the context of lateral translation or tilt of the PSM.

Figure 7 showcases the value of the defocus Zernike coefficient z3, produced by the SKW's NN mathematical model, as a function of the axial PSM translation. This translation is toward the mirror and away from its CC where the PSM was initially focused (the axial translation origin). The black dots represent the measurements, while the dotted line illustrates the best linear fit. The line crosses zero at -1.261mm (we are intra-focal), which is close to the Zemax calculation reported above, which would be -1.215mm (we are intra-focal). The discrepancy is likely due to tolerances of some PSM components and measurement errors.

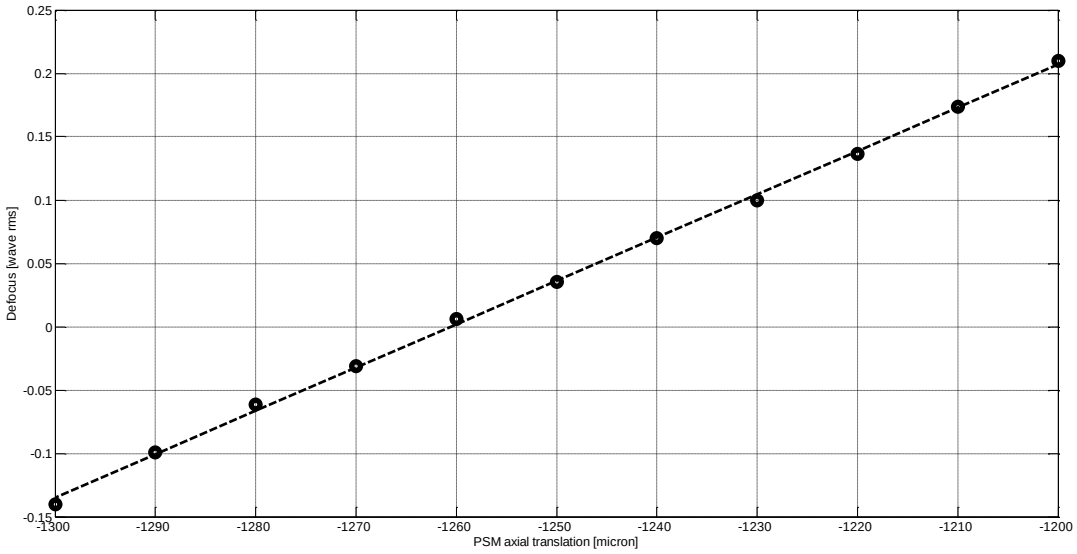

Figure 7. Defocus Zernike coefficient z3, in wave rms, versus the PSM axial translation, in micron, away from the mirror's CC and toward it. Black dots are the z3 values output by the SKW PSM NN mathematical model. The dotted line is the best fit: Slope = 0.0036 wave rms per micron, zero-crossing at -1261 microns.

The slope of the best linear fit is 0.0036 wave rms per micron, which aligns closely with the theoretical value of 0.0037 from the Zemax calculation.

Figure 8 showcases the relationship between a lateral translation of the PSM away from the mirror's center CC in the horizontal direction (measured in microns) and the horizontal coma Zernike coefficient z6 (expressed in wave rms). The black dots represent the measurements, while the dotted curve corresponds to the expected values derived from simulation. The measurements are aligned with the expected Zernike coefficient z6.

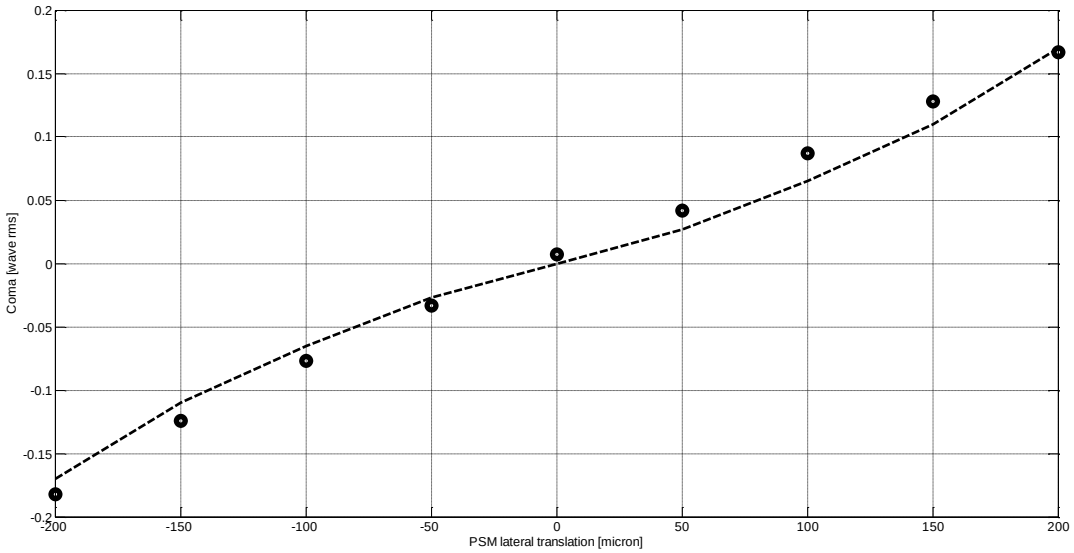

Figure 8. Horizontal coma Zernike coefficient z6, in weave rms, versus the PSM lateral translation (horizontal), in micron. Black dots are the z6 values output by the SKW PSM NN mathematical model. The dotted line is expected values form simulations.

Figure 9 displays defocused images corresponding to lateral PSM translations of 0, +100, and +200 microns. An observable shift and gradient of the image's brightest portion towards the edge is evident, indicative of coma in a Gaussian beam.

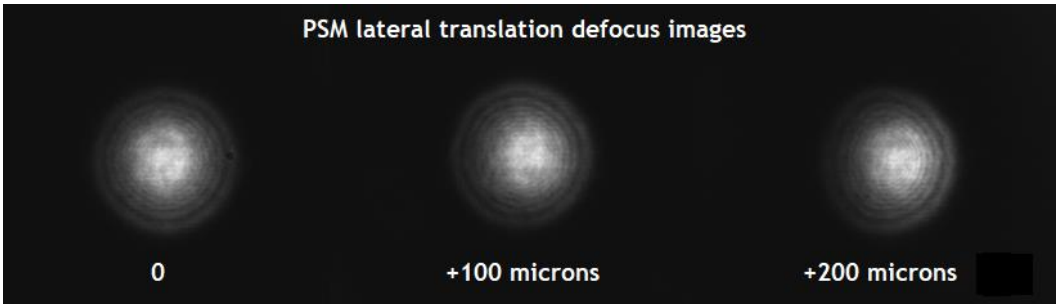

Figure 9. Defocused images for a PSM lateral translation of 0, +100 and +200 microns

5. CONCLUSIONS

Despite being initially designed and optimized for telescopes, the SKW software has proven to be very promising when used to measure WF with a PSM. The results presented in this paper are preliminary, proof of concept, more work needs to be done, but clearly, they indicate a great potential. The image-space WF sensing capabilities of the Artificial Intelligence WF Sensing (AIWFS) technology, as implemented in SKW, are versatile and can be adapted for many applications and configurations, provided the necessary modeling and parameterization are executed.

As a software-only solution, it is inherently flexible and cost-effective, enabling the reuse of cameras already present in many systems, like the PSM. This not only makes it a practical choice but also one that encourages sustainable use of resources which is quite critical in applications like aerospace. It's important to note that, by design, this technology provides a unique ability to perform WF sensing across the entire field of view in a single instance, using just one image,

as long as multiple defocused sources are available. This feature sets it apart by enabling comprehensive and efficient field dependent data acquisition and analysis.

The next exciting phase is the development of a dedicated PSM WF sensing software, based on the AIWFS technology. This evolution promises to further elevate the measurement and analysis capabilities with the PSM and offer an interesting, cost effective, very compact as well as flexible alternative to traditional WF sensing approaches, such as interferometry or SH sensors and alike.

REFERENCES

[1] Baudat, G., "Low-cost wavefront sensing using artificial intelligence (AI) with synthetic data", Proc. SPIE 11354, Optical Sensing and Detection VI April 1, Strasbourg, France (2020).

[2] Roddier Claude and Roddier Francois, "Wave-front reconstruction from defocused images and the testing of ground-based optical telescopes", Journal of Optical Society of America, vol. 10, no. 11, 2277-2287 (1993).

[3] Gaston Baudat, John Hayes, "A star-test wavefront sensor using neural network analysis", Proc. SPIE. 11490, Interferometry XX ,20 August 5, San-Diego, USA (2021).

[4] W. H. Steel, The autostigmatic microscope, Opt. Lasers Eng., 4, 217-27 (1983)

[5] R. E. Parks and W. P. Kuhn, Optical alignment using the Point Source Microscope, Proc. SPIE, 5877, 58770B (2005)

[6] W. Cai, D. Kim, P. Zhou, R. E. Parks and J. Burge, Interferometer calibration using the random ball test, OSA, OF&T, OMA7 (2010)